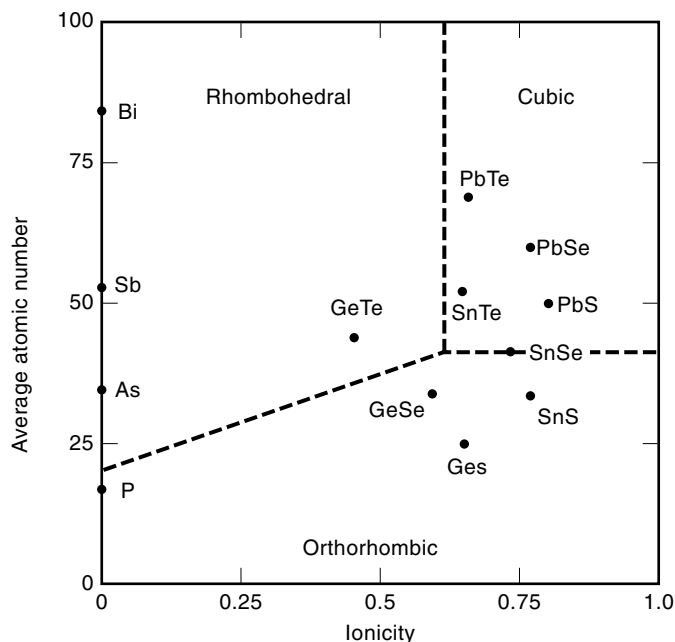# IV–VI SEMICONDUCTORS

The binary IV–VI compounds formed from elements of columns IV (Ge, Sn, and Pb) and VI (S, Se, and Te) of the periodic table of elements are among the oldest known semiconducting materials, and the most prominent representatives, such as PbS, PbSe, and PbTe, have been used for more than 100 years for electronic and optoelectronic device applications. Already in 1874, the first ever reported solid state diode was made from single crystal PbS by Ferdinand Braun (1), and its rectifying properties were exploited in the early radio receivers. Later on, the interest in the IV–VI semiconductors shifted to mid-infrared optoelectronic device applications such as photon detectors operating in the 3 to 14 μm wavelength range, taking advantage of the narrow energy gap between the valence and conduction band of the IV–VI compounds. In 1964, very soon after the demonstration of lasing in III–V semiconductor diode structures, the first mid-infrared pn-junction laser was made by Butler et al. (2) using $Pb_{1-x}Sn_xTe$. Since then, efficient mid- and far-infrared IV–VI-compound diode lasers have been fabricated, finding their main applications for remote detection of gaseous pollutants in trace-gas sensing devices, for toxic-gas analysis systems, for human breath analysis in medical diagnostics, and for fabrication process control (3). Recently, IV–VI multi-quantum-well structures have also attracted a lot of attention for their potential as efficient thermoelectric devices (4).

MATERIAL PROPERTIES

In contrast to the tetrahedrally coordinated group IV semiconductors such as diamond (C), silicon (Si), and germanium (Ge) or the III–V (GaAs, AlAs, InAs, etc.) or II–VI semiconductors (ZnTe, CdTe, etc.), there are ten instead of eight bonding electrons per atom pair in the IV–VI compounds. Whereas in the diamond or zinc-blende-type semiconductors the atoms are fourfold coordinated in the crystal lattice (four next nearest neighbors) due to the sp^3 hybridization, the six p electrons per atom pair in the IV–VI semiconductors promote a hybridization with the bonds orbitals nearly at 90° angles, resulting in a sixfold coordination of the atoms in the lattice. As a consequence, the crystal structure as well as many physical and electronic properties of the IV–VI semiconductors differ strongly from those of the tetrahedrally bonded semiconductors, but exhibit some remarkable similarities with the group V (As, Sb, Bi) semiconductors, or semimetals, which also have ten bonding electrons per atom pair. In addition, the bonding

Figure 1. Average atomic number plotted versus ionicity for the IV–VI compounds and the group V elements (5).

such as the lead, tin, and germanium oxides and the silicon chalcogenides, either crystallize in a tetragonal structure (PbO) or exist only in dichalcogenide form (SiO_2, SiS_2, $SiSe_2$, and $SiTe_2$). Thus, these compounds belong to a different class of materials, and they are not treated further in this review. Since almost all device applications of the IV–VI semiconductors are based on the materials subgroup of the cubic lead chalcogenides PbTe, PbSe, and PbS and their quasibinary alloys with other chalcogenide compounds, these will be the main focus here. Mechanically, the lead salt compounds are much softer (plastically deformable) than the tetrahedrally bonded semiconductors. This has significant implications for device fabrication processes.

Electronic Properties

A main property of the electronic band structure of the lead salt compounds is the small and direct energy gap, in the range below 600 meV (7,8). Since the maxima of the valence band and the minima of the conduction band are located at the same wave vector in reciprocal space, optical photons can be directly absorbed or emitted at the band edges. This makes the lead salts very well suited for optoelectronic applications such as photon detectors or emitters. The band extrema are located at the edges in the $\langle 111 \rangle$ directions of the Brillouin zone (L points). In contrast to most other semiconductors, the conduction and valence bands are nearly mirror-symmetric with almost equal effective masses for the electrons and holes. Because of the narrow energy gaps, the energy bands are strongly nonparabolic and the effective masses of electrons as well as holes are rather small ($0.02m_0$–$0.08m_0$ for the transverse masses). In addition, the bands are anisotropic, i.e., the Fermi surfaces are elongated ellipsoids of revolution around the $\langle 111 \rangle$ axes, characterized by a longitudinal and a transverse effective mass m^l and m^t parallel and perpendicular to the eightfold $\langle 111 \rangle$ directions. For PbTe the effective-mass anisotropy is very large, with a ratio of about 10 between longitudinal and transverse masses, whereas for PbSe and PbS this ratio is only 1.8 and 1.2, respectively.

In contrast to most semiconductors, the energy bandgap of the lead salt compounds decreases with decreasing temperature. Upon cooling from room temperature to 4 K, the energy bandgaps decrease by about 150 meV (see Table 1). This represents a quite large *relative* change with respect to the absolute value of the bandgap, and this effect is utilized for spectroscopic applications of the lead salt mid-infrared diode lasers, allowing easy tuning of the emission wavelength over a broad range just by changing of operation temperature. For adjustment of the fundamental absorption edge of lead salt infrared detectors as well as of the emission spectral region of the diode lasers, alloying of the lead salt compounds with

in the IV–VI semiconductors is not purely covalent; there is a very strong contribution of ionic as well as metallic-like bonding.

Structural Properties

In Fig. 1, the crystal structure of the IV–VI semiconductors and of the group V materials is shown as a function of ionicity and average atomic number (5). All compounds are essentially sixfold coordinated, but due to differences in the contributions of covalent, ionic, and metallic bonding, a rich polymorphism exist in these groups of materials, that is, these compounds crystallize in a variety of different crystal structures. The purely covalent group V elements exist in a rhombohedral modification due to a distortion of the simple cubic lattice along the [111] cube diagonal direction. With increasing ionicity, the preferred crystal structure of the IV–VI compounds changes from the still rhombohedral GeTe to the cubic SnTe, PbTe, PbSe, and PbS. Since the latter crystallize in the rocksalt crystal structure, these lead and tin monochalcogenides are usually referred to as lead salt compounds. The IV–VI compounds such as SnSe, SnS, GeSe, and GeS, with smaller average atomic number, crystallize in an orthorhombic structure, which has been attributed to the lower metallic contribution to their bonding (6). Other IV–VI compounds,

Table 1. Physical Properties of Some Binary IV–VI Semiconductors (9,10)

Material	Lattice Constant a_0 (Å)	Melting Point (°C)	Energy Gap E_g (meV)			Static Dielectric Const. ϵ_0		
			300 K	77 K	4 K	300 K	77 K	4 K
PbTe	6.462	930	319	217	190	414	1000	1350
PbSe	6.124	1080	278	176	147	210	227	280
PbS	5.936	1113	410	307	286	169	181	—
SnTe	6.300	806	600	360	360	—	—	1200

other chalcogenide compounds is used (11). For far infrared applications at wavelengths beyond 6 μm, the most important alloy systems are the lead–tin chalcogenide alloys. The tin chalcogenides (SnS, SnSe, SnTe) form single-phase pseudobinary alloy systems with the lead salts for all compositions (12), and they have a band structure similar to the lead salt compounds. However, since the arrangement of valence and conduction bands is exchanged, with increasing Sn content of the ternary lead–tin chalcogenide alloys the energy bandgap decreases, and a zero-bandgap semiconductor is reached for a Sn content of $x_{Sn} \approx 40\%$ in $Pb_{1-x}Sn_xTe$, and of $x_{Sn} \approx 20\%$ in $Pb_{1-x}Sn_xSe$, at a device operation temperature of 77 K. To obtain larger bandgaps and smaller cutoff wavelengths, the lead salt compounds can be alloyed with various other group IV, IIa, or IIb, Mn, or rare earth chalcogenides as shown in Fig. 2 (11). Thus, a wide spectral region from 0 to 1 eV can be covered with the IV–VI semiconductor devices.

Another important property of the lead salt compounds is their huge static dielectric constant (see Table 1). This is because the lead salt compounds, in particular PbTe, are close to a structural phase transition from the cubic to a rhombohedral phase (see Fig. 1) that exhibits pronounced ferroelectric properties. In fact, the binary IV–VI compounds GeTe and SnTe are ferroelectric at temperatures below their Curie temperatures θ of 700 and 145 K, respectively, The ternary compounds $Pb_{1-x}Ge_xTe$ and $Pb_{1-x}Sn_xTe$ also become ferroelectric at low temperatures for Ge or Sn contents as small as about 1 and 20%, respectively (13). Thus, although PbTe remains cubic for all temperatures, the temperature dependence of its static dielectric constant $\epsilon_0 \propto C/(T - \theta)$ can be associated with an extrapolated negative Curie temperature θ of -75 K, i.e., the static dielectric constant strongly increases as the temperature decreases, reaching a value of $\epsilon_0 = 1350$ at 4 K.

As a result of the large dielectric constants and the effective screening of charged impurities, the scattering of carriers at ionized impurities is rather weak in the IV–VI compounds.

This leads to very high electron and hole mobilities at low temperatures, where the mobility is mainly limited by ionized impurity scattering, while the room temperature mobilities are comparable to that of silicon. In fact, for PbTe low-temperature carrier mobilities of several times 10^6 cm^2/Vs have been observed (14). In addition, due to the large dielectric constants, the carrier binding energies at shallow donors or acceptors are extremely small, so that no carrier freeze-out is observed in the lead salt compounds even at very low temperatures. The effective screening makes the IV–VI materials much less sensitive to defects and impurities introduced during crystal growth or by device fabrication processes. As a result, high-quality IV–VI epitaxial layers have been obtained already by relatively simple deposition techniques, in contrast to the situation for the group IV, III–V, or II–VI semiconductors. Another important aspect is the comparatively low thermal conductivity of the lead salt compounds. While this is favorable with respect to the performance of thermoelectric cooling elements, it causes problems in the removal of dissipated heat in high-power diode lasers.

Optical Properties

Among the semiconducting elements and compounds, the peculiar band structure of the lead salts leads to particularly high values of the absorption constant and refractive indices in the frequency range of the fundamental absorption, a fact that is important for their use as infrared detectors and emitters. The strong absorption of photons with energies above the fundamental energy gap is due to the particularly high joint density of states at the direct energy gap at the L points of the Brillouin zone. This is one of the main advantages of the lead compounds compared to the III–V or II–VI narrow-gap semiconductors such as InSb, or HgCdTe with the direct gap at the Γ point of the Brillouin zone. While the transverse effective masses of the carriers in the IV–VI compounds are
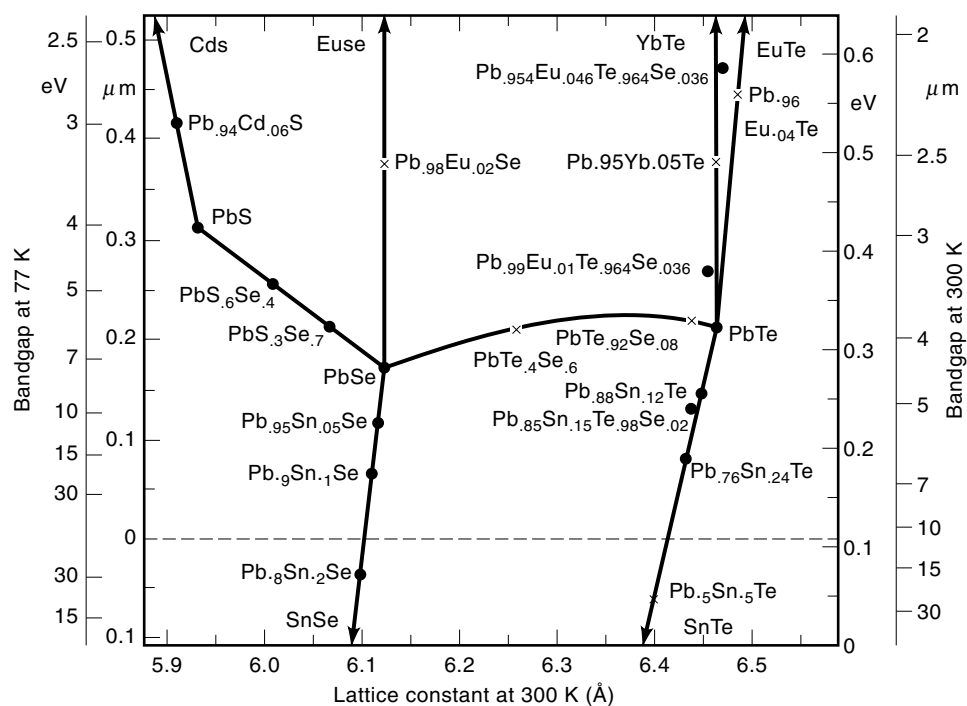
Figure 2. Energy bandgap versus lattice constant for the IV–VI semiconductors.
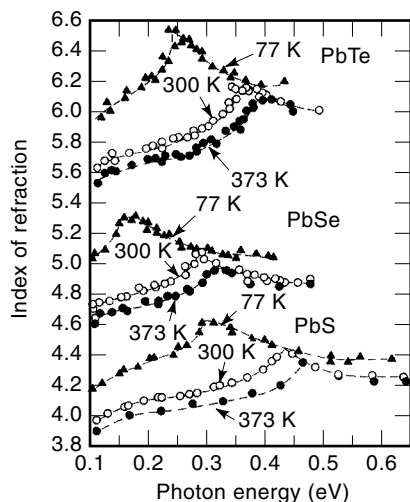
Figure 3. Refractive indices of PbTe, PbSe, and PbSe as a function of photon energy at 77, 300, and 373 K (16).

comparable to that of the narrow-gap III–V and II–VI compounds, their longitudinal effective masses are much larger, which together with the fourfold valley degeneracy at the L point of the Brillouin zone leads to a substantially higher joint density of states for electronic transitions between the valence and conduction bands and thus to much more efficient photon absorption.

The optical absorption A and reflection R as functions of frequency ω are linear optical processes described within the framework of the frequency-dependent dielectric function $\epsilon(\omega)$. This function describes the linear response of a medium to electromagnetic radiation. The refractive index $n(\omega)$ and the absorption index $\kappa(\omega)$ [with the absorption constant $\alpha(\omega) = 4\pi\kappa/\lambda$, where λ is the wavelength of the electromagnetic radiation in vacuum] are related to the real and imaginary parts of the dielectric function as $\epsilon_1(\omega) = n^2 - \kappa^2$ and $\epsilon_2(\omega) = 2n\kappa$. The dielectric function contains contributions from the optical response of the free carriers, characterized by a plasma frequency ω_p, contributions from the infrared active lattice vibrations (phonons), and contributions from the electronic interband transitions. The first two parts are of relevance mainly in the far- and mid-infrared region, whereas close to the energy gap the fundamental absorption due to electronic transitions between states involving the top valence band and the lowest conduction band at the L points of the Brillouin zone dominates $\epsilon(\omega)$ and the absorption and reflectivity spectrum. For still higher photon energies, $\epsilon(\omega)$ is determined by the contributions from other electronic transitions at critical points with high joint density of states (15).

Since $\epsilon_1(\omega)$ and $\epsilon_2(\omega)$ are related through Kramers–Kronig relations (KKRs), the same holds for the refractive and absorption indices. Due to the rapid increase of $\alpha(\omega)$ for photon energies larger than the fundamental gap, $n(\omega)$ exhibits a pronounced peak at the onset of these transitions. This is shown in Fig. 3 for PbTe, PbSe, and PbS (16). The shift of these peaks with temperature to higher photon energies reflects the temperature dependence of the energy gaps of the lead salt compounds as described in the previous section. The direct energy gaps E_g are at somewhat lower positions than the

maxima in $n(\omega)$, as follows from the properties of the KKR transformation.

In two-dimensional quantum well structures the changes of the absorption constant with frequency are particularly steep for energies that correspond to the onset of absorption between quantum confined electric subbands in the valence and conduction bands. Figure 4 shows as an example the measured optical transmission (dashed curve in center panel) of a PbTe–PbEuTe multi-quantum-well (MQW) structure on a (111)-oriented BaF$_2$ substrate as a function of frequency in
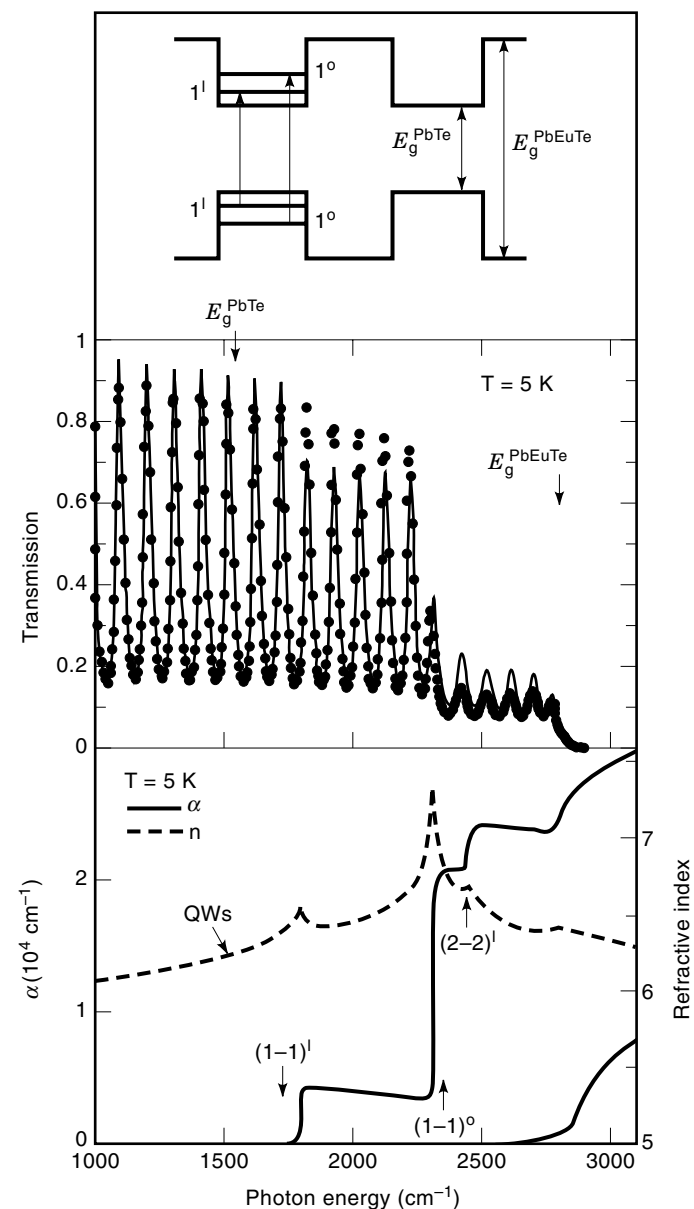
Figure 4. Measured and calculated infrared transmission of a PbTe–PbEuTe multi-quantum-well structure grown on a (111)-oriented BaF$_2$ substrate (dots and full line in the center panel), and corresponding energy-dependent absorption $\alpha(\omega)$ and refractive index $n(\omega)$ (lower panel). Interband transitions between electric subbands in the PbTe quantum wells involving longitudinal and oblique valleys (as explained in the schematic diagram of the upper panel) are indicated by the arrows at the absorption and refractive index spectra (17).

the vicinity of the fundamental bandgap. As the photon energy increases, a steplike decrease of the optical transmission takes place whenever the photon energy exceeds the energy separation between the confined quantum well electronic states in the valence and conduction bands, as indicated in the upper panel of Fig. 4 (17). Superimposed on this are Fabry–Perot interference fringes due to multiple reflection of the optical waves at the surface and the MQW–BaF_2 interface.

In the transmission spectrum, the energetic positions of the bandgaps of the well material PbTe and the barrier material PbEuTe of are indicated by arrows, and the full curve represents results of a numerical transmission calculation (17). The energy dependence of $\alpha(\omega)$ and $n(\omega)$ derived from the calculations is shown in the lower panel of Fig. 4. For the growth of the MQW structure along a $\langle 111 \rangle$ direction, two sets of subbands are formed: one associated with the valleys of constant energy oriented with the main axis parallel to the growth direction (longitudinal valley, denoted by l in Fig. 4), and one for the valleys oblique (o) to it. The latter electric subbands correspond to threefold-degenerate states. The nomenclature for the interband transitions is indicated in the schematic diagram shown in the upper panel of Fig. 4. Due to the threefold degeneracy of the oblique valleys, the steplike changes in $\alpha(\omega)$ are much larger for transitions involving electronic states of the oblique valleys than for those involving the longitudinal valley (see Fig. 4, lower panel). Correspondingly, also the cusplike enhancements of the refractive index are much larger for the $(1-1)^o$ transitions than for the $(1-1)^l$ or $(2-2)^l$ transitions, which is important for the proper design of MQW laser structures.

Doping

For doping of the lead salt compounds two alternative methods can be used, namely, (1) adjustment of the crystal stoichiometry, or (2) doping with various kinds of impurities. The first technique is based on the fact that the IV–VI monochalcogenides can accommodate small deviations from the exact $1:1$ stoichiometry by formation of vacancies or interstitials (18). Since the electronic states of these vacancies are resonant within the conduction or valence bands, each metal (Pb or Sn) vacancy acts as doubly charged acceptor, and each chalcogen (Te, Se, or S) vacancy acts as doubly charged donor (19). As a consequence, the simplest way to adjust the carrier concentration in IV–VI materials is by annealing in vacuum or under chalcogen atmosphere. In thin film deposition, doping can be achieved by supply of excess group IV or group VI flux during growth. On the other hand, because of this, background doping levels below 10^{17} cm^{-3} are difficult to achieve in the lead salt materials. For doping with impurities, atoms from group IIIa (In, Ga, Tl), group Va (As, Sb, Bi), and group Ib elements (Cu, Ag) have been used (20,21). Most of these dopants are amphoteric p- or n-type, depending on whether the impurities are incorporated substitutionally on metal or on chalcogen lattice sites. The latter depends significantly on the growth conditions. Tl, Ag, and Bi have proven to be most efficient as dopants. These dopants incorporate well into the crystal lattice under chalcogen-rich conditions with a unity doping efficiency for doping levels as high as 10^{20} cm^{-3}. When occupying substitutional metal lattice sites their doping action is readily understood from the fact that the acceptors Tl and Ag have one electron less, whereas the donor Bi has one valence electron more, than Pb or Sn.

CRYSTAL GROWTH AND THIN FILM DEPOSITION TECHNIQUES
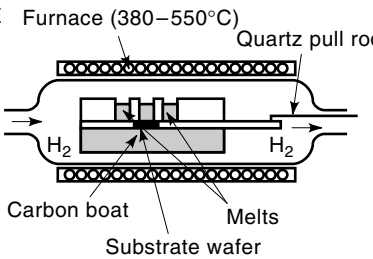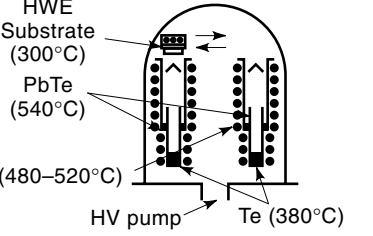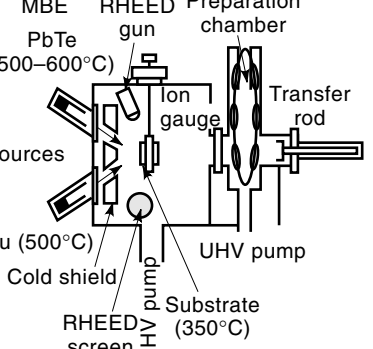
Growth of Single Crystals

For IV–VI-compound diode lasers as well as thermoelectric devices, high-quality bulk single crystals are required. Diffused homojunction laser diodes can be made directly from binary and ternary single crystals, where the choice of composition allows the adjustment of the emission wavelength. However, higher laser operating temperatures have been achieved only by fabrication of double heterostructure (DH) lasers, where the active thin film laser structure is deposited epitaxially on a lead salt single crystal substrate.

Since the melting points of the lead and tin chalcogenides are only moderately high (around 1000°C), many different crystal growth techniques can be used to obtain single crystals (21,22). Comparatively large single crystals can be pulled from the melt by the Czrochalski or the Bridgman method, but the residual dislocation densities in the crystals are rather high (10^5 to 10^7 cm^{-2}), and such grown ternary single crystals show significant inhomogeneities in alloy composition. Single crystals grown by vapor phase transport techniques exhibit the highest structural perfection, with much lower dislocation densities in the range 10^2 to 10^4 cm^{-2} and with much better compositional homogeneity of ternary single crystals. Therefore, the latter is the preferred technique for the fabrication of laser materials, although the crystal growth rates are rather low. High-quality PbTe single crystals have also been grown using the traveling heater method, where a solvent-rich molten zone is slowly moved across a Bridgman-grown ingot. This leads to very high-purity single crystals due to the zone refining effect and due to low impurity concentrations as a result of the low growth temperatures. Using either lead or chalcogen as solvents, p- or n-type single crystals with excellent homogeneity have been prepared.

Epitaxial Thin Films

Thin films of IV–VI semiconductors are used for infrared photon detectors as well as for laser diodes. For the photodetectors, thin films are deposited on various substrate materials such as mica or BaF_2. For commercially available low-cost infrared detectors, polycrystalline thin films are sufficient, which are prepared either by vacuum deposition or by precipitation from aqueous solutions. For the fabrication of high-quality epitaxial layers and heterostructures three main growth methods have been used, namely, liquid phase epitaxy, hot wall epitaxy, and molecular beam epitaxy (23,3). These methods and their advantages and disadvantages are summarized in Fig. 5.

In liquid phase epitaxy (LPE), the layer growth occurs on a substrate in direct contact with supersaturated melts contained in graphite wells (see Fig. 5). The thin film growth rates are controlled by the lowering of the melt temperature. Heterojunctions or multilayers can be grown by subsequent position of the substrate slider under different wells with different melt composition. In order to prevent contamination with unwanted impurities, the growth is carried out in a hy-

Methods	Advantages	Disadvantages
LPE Furnace (380–550°C) Quartz pull rod H$_2$ H$_2$ Carbon boat Melts Substrate wafer	Simple Cheap	Rare earth materials difficult Compositional change with time Limited no. of layers No thichness control
HWE Substrate (300°C) PbTe (540°C) Eu (480–520°C) HV pump Te (380°C)	Moderate price High-quality layers	Compositional control difficult No *in situ* quality control (RHEED)
MBE RHEED gun Preparation chamber PbTe (500–600°C) Ion gauge Transfer rod Sources Eu (500°C) UHV pump Cold shield RHEED screen UHV pump Substrate (350°C)	High flexibility Flux control Lattice-matched layer structures possible Control of doping concentration	Very expensive Small growth rate

Figure 5. Epitaxial growth techniques used for IV–VI compounds. Top: liquid phase epitaxy (LPE), middle: hot wall epitaxy (HWE), bottom: molecular beam epitaxy (MBE) (3).

drogen atmosphere. LPE has been used for the fabrication of far-infrared heterojunction laser diodes with Pb$_{1-x}$Sn$_x$Te or Pb$_{1-x}$Sn$_x$Se as active regions. The rather high growth temperatures, however, result in significant alloy interdiffusion at the heterojunctions, i.e., to a smearing of the compositional profiles between the different layers.

In hot wall epitaxy (HWE) (24), the epitaxial layers are grown from the vapor phase under high-vacuum conditions. The different source materials are contained and sublimed in a quasiclosed quartz tube with well-defined temperature gradients along the tube axis. The flux of the sublimed source materials is guided by the hot walls of the tube to the substrate placed at the end of the tube and held at a somewhat lower temperature around 300 to 400°C in order to condense the epitaxial layer. For the growth of ternary alloy layers several different temperature zones can be incorporated in a hot wall tube for sublimation of the different constituents of the layers. The composition and the carrier concentration in the layer can then be adjusted by varying the actual sublimation temperatures in the different zones. Multilayers or heterojunctions are prepared by combining several hot wall tubes in a single vacuum chamber and by moving the substrate from one tube to another for the growth of each individual layer (see Fig. 5). With HWE very high-quality epitaxial layers and multilayer structures of various IV–VI material systems have been fabricated, and different types of heterojunction diode lasers have been successfully made.

Molecular beam epitaxy (MBE) is the most advanced and versatile epitaxial growth technique for fabrication of complicated IV–VI multilayer heterostructures (11,25,26). In MBE, molecular beams of the constituent materials are generated by evaporation from effusion cells and directed on a heated substrate, where the epitaxial layer is grown (see Fig. 5). For the growth of multilayers and heterostructures, the molecular beams can be rapidly switched on and off by mechanical shutters in front of the effusion sources. In the ultrahigh-vacuum chamber of the MBE system up to eight different effusion cells for various source materials are included, and thus layers of different constituents and dopand elements can be prepared in one system and a single growth run. The chemical composition of ternary or quaternary alloy layers as well as the dopand concentration can be adjusted by appropriate setting of the flux rates from the different effusion sources. Flux rate control is achieved by using an ion gauge or quartz-crystal microbalance beam-flux monitors. Because of the fast switching between the different molecular beams and because of the comparatively low growth temperatures, abrupt interfaces between the individual layers can be obtained. In order to obtain very high-purity layers, epitaxial growth is carried out under ultrahigh-vacuum conditions. In situ control of the growing surface is routinely achieved by reflection high-energy electron diffraction. Due to the excellent control of layer thicknesses, compositions, and carrier concentration profiles in complicated multilayer structures, MBE is the method of

choice for the fabrication of IV–VI multiple quantum wells, superlattices, and advanced devices such as heterostructure *pn* junction lasers, the last of which are produced by MBE on a commercial basis.

Since high-quality single crystal IV–VI substrates are extremely expensive and not commercially available, many different materials (NaCl, KCl, BaF$_2$, Si, GaAs, etc.) have been used as substrate materials for epitaxial IV–VI layers (26). However, the usual semiconductor substrates such as (100)-oriented Si or GaAs do not have well-matched lattice constants, and the thermal expansion coefficients are quite different from that of the IV–VI compounds. As a result, epitaxial growth on these substrates results in a high dislocation density in the layers, and thermal cycling of IV–VI infrared devices to cryogenic operation temperatures causes large thermal strains in the layers, which lead to defect generation and to a degradation of the electronic properties of the layers. In this respect, BaF$_2$ is the best choice of non-IV–VI substrate material, since its thermal expansion coefficient is essentially equal to that of the IV–VI compounds. Recently, however, high-quality IV–VI epitaxial layers have been grown on (111)-oriented Si substrates using thin CaF$_2$–BaF$_2$ layers as buffer layers, and it was demonstrated that for growth on (111)-oriented Si substrates the thermal strains can be effectively relaxed by dislocation slip processes without dramatic degradation of the electronic properties of the layers (26).

BANDGAP ENGINEERING

For optoelectronic applications as well as quantum confined low-dimensional heterostructures, the adjustment of the fundamental bandgap of the materials used is of crucial importance. This bandgap engineering is generally achieved by alloying of materials with different bandgaps. In these alloys, the energy bandgap can then be tuned by adjustment of the alloy composition. As illustrated in Fig. 2, in the IV–VI semiconductor system many different ternary and quaternary alloys have been used for this purpose (11). Of the classical alloys among the IV–VI compounds, the ternary PbTe–SnTe and PbSe–SnSe single-phase alloys have been used for far-infrared applications. Since the conduction and valence levels in the tin chalcogenides are exchanged with respect to the lead chalcogenides, the bandgap of the ternary alloy decreases linearly with increasing Sn content, reaching zero for a certain alloy composition. Other pseudobinary IV–VI alloys with exchanged group IV (e.g., Pb–Ge) or group VI element (e.g., Se–Te) are less useful, since the achievable variations of the bandgap energies are comparatively small while the lattice constants change rather strongly with varying alloy composition. Among such alloys, the largest tuning range can be achieved in the PbSe$_{1-y}$S$_y$ system with a bandgap variation from 172 to 310 meV at 77 K. Since other IV–VI compounds such as SnS, GeTe, or GeSe do not crystallize in the rocksalt crystal structure, only a very limited miscibility regime exists for their alloys with the lead salt compounds. The same applies also for alloys with MnTe or CdTe. Only Pb$_{1-x}$Cd$_x$S exhibits a relatively wide miscibility region, and shorter-wavelength IV–VI diode lasers have been fabricated in this alloy system.

In order to obtain higher-bandgap materials, alloys of the lead salts with rare earth monochalcogenides (EuTe, EuSe, EuS, YbTe, SmTe, etc.) or alkaline earth chalcogenides (SrTe, SrSe, SrS, BaTe, BaS, CaTe, CaS) have been used (11). These compounds share the same rocksalt crystal structure as the lead salt compounds. Of the rare earth monochalcogenides most are metallic, with the exception of those with the divalent rare earth elements Eu, Yb, Sm, and Tm. The corresponding highly ionic monochalcogenides are semiconductors with energy bandgaps in the 1 to 2 eV range. The Eu chalcogenides are the ones with most stable rare earth ion in the 2+ state, due to the half-filled atomic 4*f* shell. Thus, complete miscibility exists for the Pb$_{1-x}$Eu$_x$X systems (X = Te, Se, S), which yields a bandgap tunability of more than 1.5 eV. The lattice constants as well as energy bandgaps of the Pb$_{1-x}$Eu$_x$X alloys depend nonlinearly on Eu content. For Eu contents below about 10%, the change in energy bandgap is very large, with dE_g/dx = 3.5, 3.0, and 5 eV for Pb$_{1-x}$Eu$_x$Te, Pb$_{1-x}$Eu$_x$Se, and Pb$_{1-x}$Eu$_x$S, respectively, with little change in the lattice constants (26). Consequently, Pb$_{1-x}$Eu$_x$X alloys have been the most widely used high-energy-bandgap alloys for lead-salt-based heterostructures and devices (27–29). Other alloys such as Pb$_{1-x}$Yb$_x$Te, Pb$_{1-x}$Sm$_x$Te, or Pb$_{1-x}$Tm$_x$Te are less useful for device applications, since Sm, Yb, and Tm can become electrically active or induce deep levels within the bandgaps (11) of the alloy material.

The alternative group of materials for high-energy-bandgap alloys are the alkaline earth chalcogenides (30). These compounds, such as CaX and SrX, have energy bandgaps above 4 eV and lattice constants comparable to that of the lead salt compounds. For the alloys Pb$_{1-x}$Ca$_x$S and Pb$_{1-x}$Sr$_x$S complete miscibility exists, and for Pb$_{1-x}$Ca$_x$Te, Pb$_{1-x}$Sr$_x$Te, and Pb$_{1-x}$Sr$_x$Se solid solutions have been obtained for Sr or Ca mole fractions at least up to 15% (11). For alloys with other alkaline earth chalcogenides such as BaTe or MgTe, only a very small solubility region exists. In the lead–alkaline-earth chalcogenide alloys, again the energy bandgap increases very rapidly with alkaline earth content, with little change in the lattice constants. This makes these alloys equally well suited for the fabrication of lead-salt-based quantum well structures and MIR diode lasers (31).

One general problem associated with the high-energy-bandgap lead salt alloys is the very rapid deterioration of the electrical properties of the epitaxial layers with increasing rare earth or alkaline earth content (26,27). In fact, for all of these alloys a similar decrease of the low-temperature electron mobility by more than two orders of magnitude has been observed already for alloy compositions of only 10%. This has been explained by very strong alloy scattering of the charged carriers (26), which can even lead to a disorder-induced metal-to-insulator transition.

INFRARED DETECTORS

Photoconductive Devices

Since about 1930 the photoconductive properties of PbS and PbSe have been used for the detection of infrared radiation. These detectors are still mass-fabricated either by vacuum deposition or by precipitation from aqueous solution in the presence of an oxidizing agent. The polycrystalline films, deposited on cheap glass or similar substrates, are usually about 1 μm thick with grain sizes of about 1 μm. The spectral characteristics of such lead salt MIR detectors compared with other
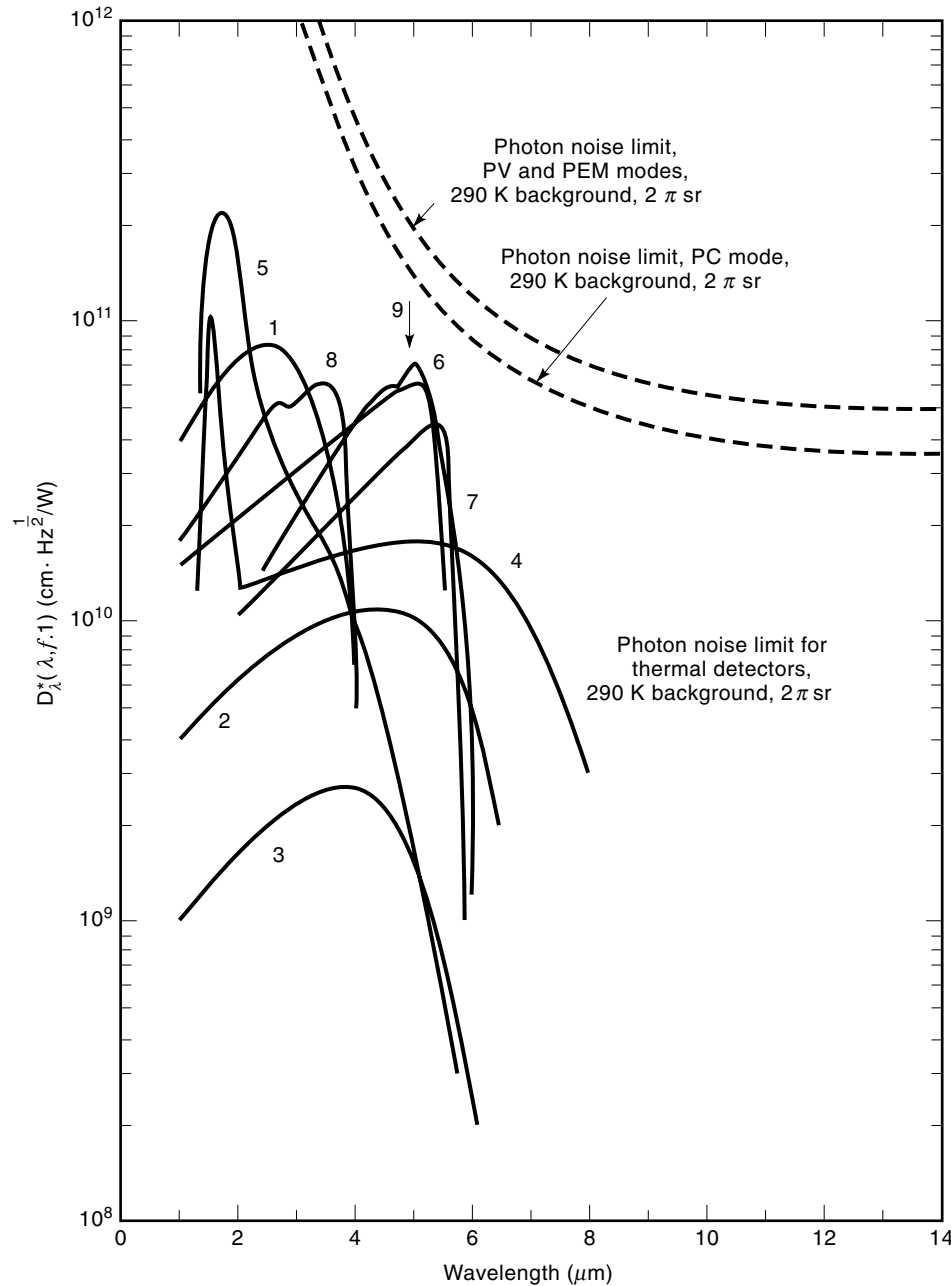
Figure 6. Spectral dependence of the detectivity D^* of various detector materials at an operating temperature of 77 K: 1, PbS; 2, PbSe; 3, PbTe; 4, Ge : Cu; 5, Ge : Au; 6, InSb; 7, InSb (photovoltaic); 8, Te. Curve 9 represents experimental data for a PbTe photoconducting doping superlattice at $T = 80$ K (32).

semiconductor detectors are shown in Fig. 6. The detectivity D^* is determined by the voltage or current sensitivity (V/W or A/W) as well as the noise level per unit frequency interval.

Apart from polycrystalline thin film detectors, also single crystal films have been used for infrared detection. In particular, the photoconductive response of a sequence of n- and p-doped PbTe multilayers (so-called *nipi* structures) was shown to come close to that for the theoretical limit for D^* of an ideal photodetector at temperatures between 77 and 90 K (32).

Recently, lead selenide detectors have been used in advanced focal plane array (FPA) detectors and are commercially available as linear or bilinear FPAs with up to 526 detector elements (33). These elements are coupled to CMOS multiplexer readout circuits. The PbSe detector elements are thermoelectrically cooled, with entire power requirement for the FPAs and the cooler of less than 5 W. These structures are a low-cost alternative to the more elaborate FPAs based on HgCdTe technology.

pn-Junction Devices

The use of liquid phase, hot wall, or molecular beam epitaxy allows the direct fabrication of pn-junction photodiodes for the 8–12 μm wavelength range. $Pb_{0.8}Sn_{0.2}Te$ layers deposited on PbTe single crystal substrates with additional PbTe or PbSnTe layers deposited on top as cold filters and antireflection coatings exhibit detection efficiencies of 70% and an amplifier-noise-limited detectivity of 10^{11} cm $\cdot$ Hz$^{1/2} \cdot$ W^{-1} at 10.6 μm for an operating temperature of 77 K (34).

Schottky-Barrier Devices

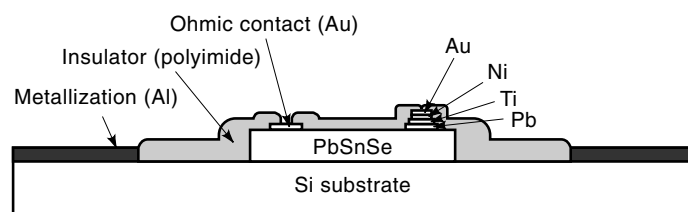Hohnke et al. (35) have demonstrated that for the atmospheric window around 10 μm another, simple lead salt

Schottky barrier technique leads to D^* values that are not much inferior to those of *pn* junction diodes. In this case *p*-type PbSnSe layers with thicknesses of about 0.5 μm are deposited by vacuum deposition or by MBE on a BaF$_2$ substrate. The Schottky barrier is made by vacuum deposition of lead (Pb). The structure is coated with polyimide for stable operation in ambient conditions. For a comprehensive review of such devices see Ref. 25.
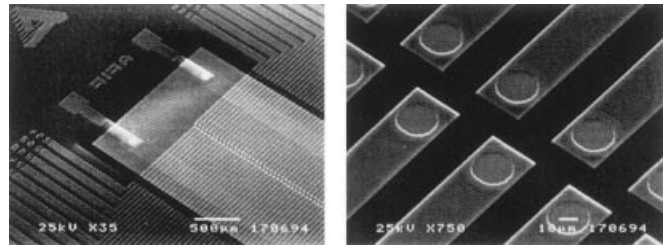
Infrared Detector Arrays on Si Substrates

The importance of thermal imaging by using focal plane arrays of many detector elements has recently stimulated further work with IV–VI epitaxial layers. In particular, the possibility of using Si substrates, as first shown by Zogg et al. (36), has brought a new impetus to the field of IV–VI infrared devices. With the use of Si wafers it is possible to integrate the detector of an infrared camera, which may consist of thousands of pixels, into the readout electronics, made from standard silicon CMOS technology. In this case, the active lead salt infrared detector elements are grown by molecular beam epitaxy on CaF$_2$–BaF$_2$ buffer layers deposited on Si (111) substrates with already fully fabricated electronic readout circuitry. In contrast, conventional HgCdTe focal plane technology relies on hybrid structures with In bump bonds between the infrared devices and the Si substrate for each of the pixels. Due to the rather high dielectric constants of the IV–VI compounds as compared to HgCdTe, the high-frequency operation of IV–VI detector structures is limited to about 100 MHz. This, however, is sufficient for infrared focal plane arrays.

For a Si-based IV–VI-compound focal plane array, first a CaF$_2$ buffer layer of about 100 Å thickness is grown epitaxially on a (111) Si wafer. On this buffer layer, a *p*-type PbSe or PbSnSe layer with carrier concentrations of about 10^{17} cm^{-2} is deposited by MBE. For reasons of heat dissipation, photovoltaic devices are preferred over photoconductive devices for infrared focal plane arrays. Therefore, the detector elements are produced by evaporation of a Pb Schottky barrier on top of the lead salt layer. This results in a blocking contact and leads to strong band bending close to the interface, acting like an induced *np* junction. A typical detector structure is shown in Figs. 7 and 8. The detectors are illuminated from the back side through the transparent Si substrate. With IV–VI active epilayer thicknesses of a few micrometers, internal quantum efficiencies close to 100% and external efficiencies of about 60% have been achieved. Common Au or Pt layers are used for the contacts, and the pitch between the detector elements is typically 50 μm. With use of either PbS, PbTe, PbEuSe, PbEuTe, or PbSnSe as detector materials, the cutoff wavelength of the detector array can be

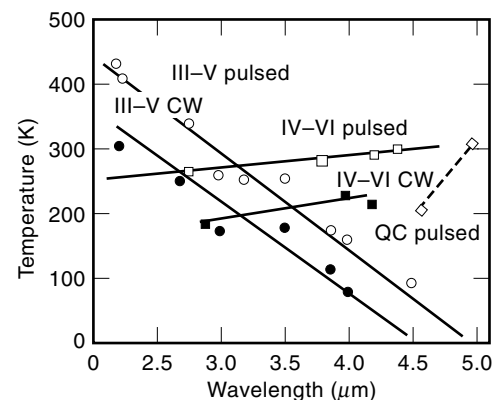

Figure 8. Scanning electron micrograph of 128 $\times$ 2 PbSnSe-on-Si infrared detector array. The pitch between sensor elements is 50 μm (36).

varied from 4 to 14 μm at $T = 77$ K. For $T < 100$ K, the sensitivity of the detector structures is limited by generation–recombination noise, whereas for higher operation temperatures these sensors are diffusion-limited. The variation of quantum efficiencies between different pixels was shown to be less than about 3% for a 256-pixel array (36). Since all growth steps for these infrared sensors are performed at temperatures below 450°C, processing compatibility exists with standard Si VLSI technology.

INFRARED DIODE LASERS

Among the infrared diode lasers, those based on IV–VI compounds play a particularly important role (29), and up to now all commercially available mid- and far-infrared laser diodes have been made exclusively from IV–VI compounds. The main material properties that are advantageous in this respect are (1) the electronic band structure, with mirrorlike bands at the L point of the Brillouin zone, resulting in high joint density of states, (2) the lower nonradiative Auger recombination rate in IV–VI compounds as compared to III–V and II–VI materials, and (3) the high dielectric constant and the resulting weak detrimental influence of defects on nonradiative recombination losses. At wavelengths longer than 3 μm, IV–VI diode lasers are superior to their III–V counterparts. As shown in Fig. 9, so far IV–VI compound lasers offer the highest CW operating temperatures at wavelengths larger than 3 μm, although the recently developed III–V-

Figure 7. Cross section of PbSnSe Schottky-barrier infrared detector on Si (111) substrate (36).

Figure 9. Maximum operation temperature of III–V- and IV–VI-compound infrared laser diodes versus wavelength. Pulsed operation: open symbols; CW operation: full symbols. QC denotes quantum cascade lasers.

based quantum cascade lasers are rapidly improving and are becoming important competitors for IV–VI lasers. The IV–VI lasers, however, are still based on conventional designs such as homojunction, heterojunction, or single and multiple heterojunction lasers.

The main applications for the IV–VI mid-infrared lasers are trace-gas-sensing systems based on laser absorption spectroscopy for pollution monitoring, factory process control, toxic-gas detection, and human breath analysis for medical diagnostics (3,37). The key absorption lines for several important atmospheric species are listed Fig. 10. Other potential applications include distance wireless communication using pulsed mid-infrared lasers, explosive detection, and differential-absorption light detection and ranging systems. The requirements for all lasers are high CW operating temperature (ultimately room temperature), reasonable output power, and in some cases single-mode operation. Among these factors, operating temperature is most important, since it influences both the price and the system complexity.

The wavelength coverage of the IV–VI layers is mainly determined by which IV–VI compounds or alloys are used. In principle, with the IV–VI lasers the wavelength range from 2.5 to about 30 μm can be covered (29). Commercially available lead salt lasers are based on either the selenide or the telluride alloy system, that is, on PbSe and its alloys or on PbTe alloys, respectively. The simplest lasers are diffused homojunction lasers, which are still used for the longer-wavelength region as shown in Fig. 10. These homojunction lasers produce so far the highest CW output powers: about 24 mW at 4.75 μm and $T = 20$ K, and 19 mW at $T = 30$ K. The output power of homojunction lasers decreases rapidly with increasing temperature. Thus, for higher operating temperatures double-heterojunction (DH) lasers are used. In a DH laser the active recombination zone for the carriers is confined to a length of about 1 μm through the presence of a larger-bandgap barrier material on both sides. These barriers prevent outdiffusion of carriers from the active zone. In addition, optical confinement of the electromagnetic wave is achieved through the lower index of refraction of the barrier material.

Whereas PbSe–PbSnSe and PbTe–PbSnTe DH lasers were made for the long wavelength range, a considerable improvement was achieved by the use of PbEuSeTe cladding layers

in DH lasers with PbTe as the active material, and of PbEuSe for PbSe-based lasers (27). The growth techniques for the fabrication of DH lasers were summarized in the previous sections.

In order to obtain a carrier and optical confinement also in the lateral direction, various stripe-geometry laser structures have been used (29). The metal stripe geometry, where a metal stripe is deposited on the laser structure, is simple to fabricate but does not offer effective lateral optical confinement. In contrast, junction stripe, mesa, or buried-heterostructure concepts offer good confinement of the carriers as well as of the optical wave. A typical DH laser structure (3) is shown in Fig. 11. In this case, a heavily doped PbTe buffer layer is deposited on a p-type PbTe single crystalline substrate, followed by the Tl-doped PbEuSeTe confinement layer, the active PbTe layer, a second Bi-doped PbEuSeTe confinement layer, and an n^+-doped PbTe cap layer. Metal contacts are evaporated on the highly doped PbTe cap layers, and insulating layers are produced by anodic oxidation of PbTe. The current is confined to the narrow stripe region by mesa etching. Further improvements in the lasers were made by fabricating separate buried-heterostructure confinement lasers, achieving the highest CW operation temperature of 223 K reported so far for IV–VI compound lasers (38). The fabrication of these lasers requires a two-step growth process, with a second MBE growth step on a photolithographically defined nonplanar surface. As with III–V lasers, distributed feedback lasers were also realized from IV–VI materials by etching a Bragg reflector grating into the top layer of the structure. An example for such a structure is shown in Fig. 12.

Of the PbSe-based DH lasers, PbSe–PbSrSe lasers were shown to have superior properties to PbSe–PbEuSe lasers due to the improved p-type doping behavior of PbSrSe. At present such lasers exhibit the highest pulsed operating temperatures of 290 K, close to room temperature (31). Several attempts have been made to improve the properties of IV–VI-compound lasers by using quantum wells as active regions in order to achieve lower threshold currents and higher operating temperatures. Single- as well as multiple-quantum-well lasers based on PbTe, PbSe, and PbS with confinement layers of PbEuSeTe, PbEuSe or PbSrSe, and PbEuS have been successfully produced. MQW lasers of PbSe–PbSrSe with seven periods of 50 nm wide PbSe wells were shown to yield maximum operating temperatures of 282 K at a wavelength of 4.75 μm (28). However, so far the improvements due to quantum confinement effects demonstrated so successfully for III–V lasers at shorter wavelengths, have not yet been achieved for the long-wavelength IV–VI lasers. An important problem is high losses due to free carrier absorption in the mid infrared.

A unique property of lead salt laser diodes is the ease of tuning of the emission wavelength due to the strong change of bandgap of the IV–VI materials with increasing temperature. This, together with their narrow linewidths, makes these lasers ideally suited for high-resolution spectroscopic applications, including scientific research in molecular spectroscopy of ions or radicals in heterodyne and acoustic spectroscopy, or Doppler spectroscopy of molecular beams (3,37). So far the main applications are time-resolved combustion analysis in the automotive industry (Fig. 13), the monitoring of emissions of power plants, exact monitoring of gas compositions in
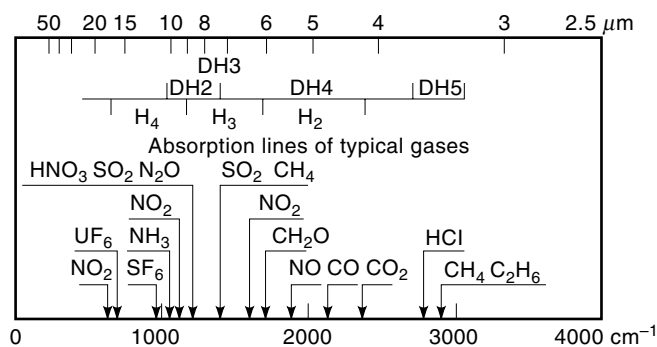
Figure 10. Typical operation wavelengths of commercially available double-heterostructure (DH) and homojunction (H) lead salt diode lasers and corresponding absorption lines of various gas molecules. Active material for DH2 and H4: PbSnSe; for DH3: PbSe; for DH4, DH5, and H2: PbEuSe. (From Laser Components, IR laser diode brochure, 1997.)
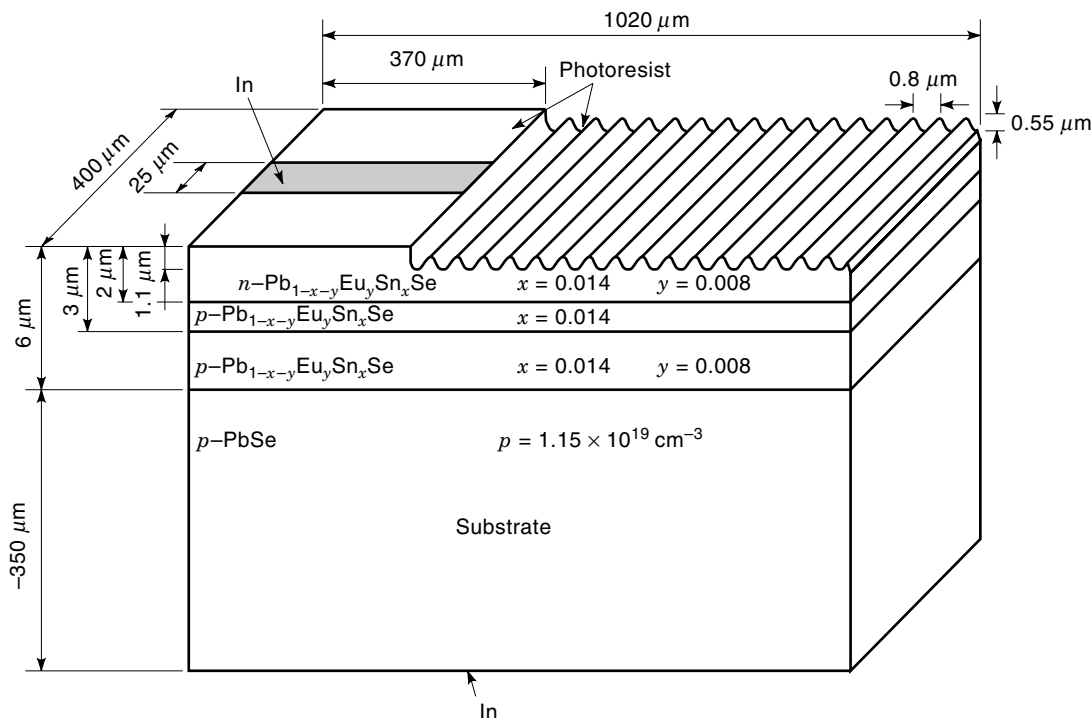
Figure 11. Schematic illustration of a PbEuSeTe–PbTe double-heterostructure stripe-geometry diode laser grown by molecular beam epitaxy (3).

Figure 12. Schematic illustration of a distributed Bragg-reflector heterojunction PbEuSnSe–PbSeSe laser structure (3,29).

chemical plants, and spatially resolved as well as time-resolved in situ analysis.
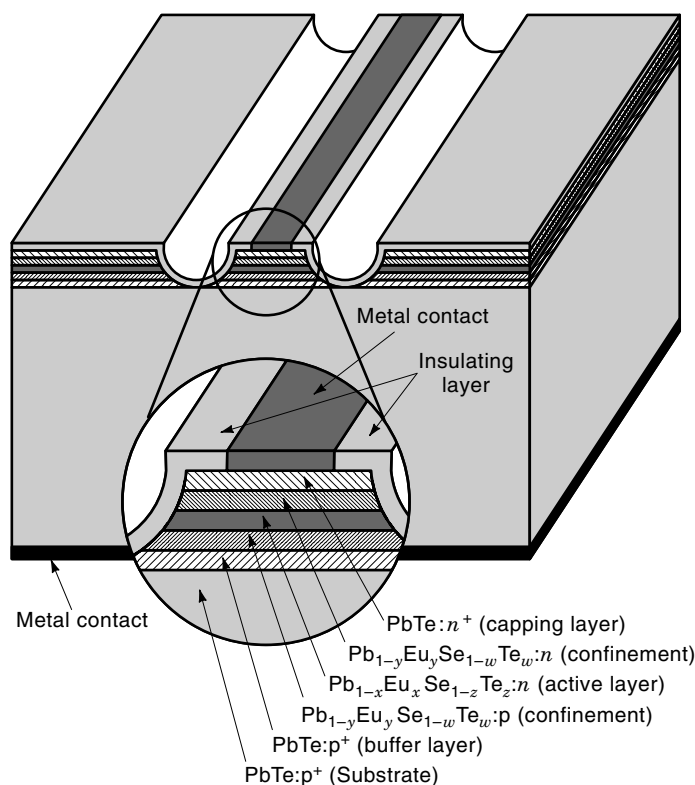
Up to now, the applications of lead-salt-based MIR diode lasers have been limited mainly by the following problems:

1. *Cryogenic operating temperatures.* For operation at 80 to 120 K, liquid nitrogen dewar assemblies are available now, but operation at temperatures reachable with thermoelectric coolers would be more convenient and stable.
2. *Discontinuous tuning range and multimode operation.* This requires the use of expensive and bulky monochromators in spectroscopy applications.

The total output power of a typical lead salt laser is about 1 mW, with several hundred microwatts per mode. This is sufficient for high-resolution spectroscopy and gas monitoring, but higher output powers will be needed for some future applications. Mode behavior is of importance for spectroscopic applications. At present, the commonly available lead salt lasers have a temperature tuning rate of a few cm^{-1}/K, and can be tuned quasicontinuously over a range of about 100 cm^{-1}. Multimode operation and mode hopping are the main problems to be solved. Progress has been made by making BH and distributed Bragg reflector (DBR) lasers (3,29).

Due to the understanding and controlling of chaotic frequency emission in IV–VI-compound tunable diode lasers by using newly developed techniques (occasional proportional feedback), new applications in high-resolution spectroscopy as well as in the use of such lasers as local oscillators for heterodyne radiometers have become possible (41).

In the last few years there has been renewed interest in mid-infrared lasers. Currently, most lasers rely on direct
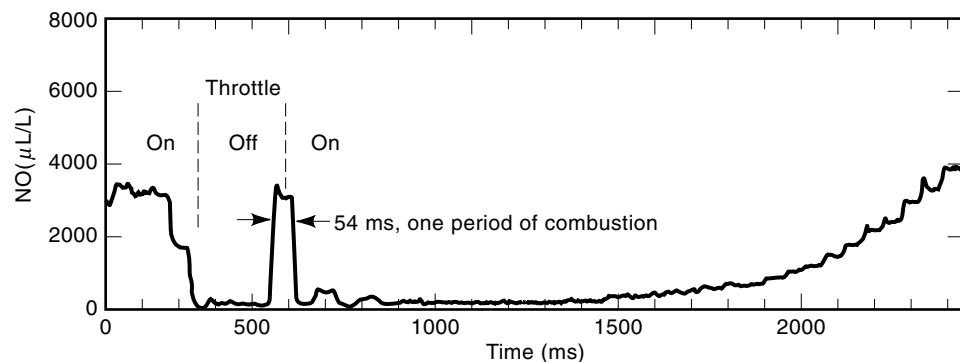
Figure 13. Example of time-resolved NO detection in the exhaust line of a car engine using a lead salt diode laser. (From Laser Components, IR laser diode brochure, 1997.)

band-to-band transitions such as in the IV–VI and III–V antimonide lasers. Other mid-infrared lasers based on new types of transitions, such as the quantum cascade lasers (39) and the type II QW lasers (40), have made promising progress. Thus, there is stiff competition between the different materials systems. For further improvements of IV–VI lasers several aspects need to be addressed:

1. Reduction of the carrier concentration in the active layer in order to reduce the losses due to free carrier absorption.

2. Improvements of the confinement layers in DH lasers, since the carrier mobility decreases exponentially as the bandgap of the confinement materials increases.

3. The thermal conductivity of IV–VI materials is low, which means a greater chance for overheating of the lasers. Reducing the volume Joule heating or the total thickness of the laser structure might improve the heat transport, which would allow an increase in CW operating temperature and in output power.

4. The quality of IV–VI substrates, with dislocation densities of typically 10^4 cm^{-2}, needs to be significantly improved. The use of other than IV–VI substrates may yield the better substrate quality and better thermal dissipation.

In the future of mid-infrared lasers, III–V quantum cascade lasers may have the best chance to reach high-temperature operation. Also, III–V antimonide-based lasers may share the market with the IV–VIs in the 3 to 4 μm region. Nonetheless, with regard to the application requirements, including extremely narrow laser linewidths, ease of tuning, ease and reproducibility of fabrication, etc., there is no doubt that 3 to 12 μm IV–VI lasers will be active in the future.

THERMOELECTRIC DEVICES

Thermoelectric devices for generating electric power without any moving parts, as well as Peltier coolers for refrigeration, have been in use since the early fifties. The lead salt compounds, as well as Bi_2Te_3–Sb_2Te_3–Bi_2Se_3 and SiGe alloys, have been investigated thoroughly in the past for these applications and are in use in commercially available devices (4). Such thermoelectric devices consist of a pair of n- and p-doped semiconductor rods that are both in contact with a heat source at one of their ends and a heat sink at the other. Heav-

ily doped PbTe is one of the materials used in today's thermoelectric power generators for temperatures near 430°C, as well as in Peltier refrigerators. The efficiency of thermoelectric devices is described by a dimensionless figure of merit ZT, which is deduced from consideration of the relationship between the electrical current and heat flow in a conducting solid.

In general, the current density $\boldsymbol{j}$ due to an applied electric field $\boldsymbol{E}$ and a temperature gradient ∇T along the conductor is given by $\boldsymbol{j} = \sigma(\boldsymbol{E} - S \nabla T)$, where σ is the electrical conductivity and S is the Seebeck coefficient, defined as the average entropy per charge carrier divided by the electronic charge. On the other hand, the heat current density $\boldsymbol{Q}$ due to an electric field or a temperature gradient is given by $\boldsymbol{Q} = \sigma TS\boldsymbol{E} - \kappa \nabla T$, where κ is the thermal conductivity, to which both the mobile carriers (κ_c) and the lattice thermal conductivity κ_l contribute. The product ZT (where T denotes the absolute temperature) is given by $ZT = S^2/\kappa\rho$, where ρ denotes the resistivity ($=1/\sigma$). Consequently, a small value of the lattice thermal conductivity is favorable for achieving a high value of ZT. The ZT value for PbTe at 430°C is 1.2, which is quite high, since present thermoelectric devices have values $0.4 < ZT < 1.3$. The analysis of the expression for ZT shows that in order to maximize ZT for semiconductors, in particular κ_l has to be minimized, keeping at the same time the mobility of the carriers as well as their effective mass high. Data for the thermoelectric figure of merit Z (ZT/T) for n-type lead telluride are shown in Fig. 14 (7).

Quite recently the renewed interest in thermoelectric devices has led to the suggestion that semiconductor quantum wells would lead to an improved figure of merit. Hicks et al. (42) have shown that for carriers confined in PbTe quantum well layers with thicknesses ranging from 1.7 to 5.5 nm and with PbEuTe barrier layers with an Eu content of 7.3%, the product ZT increases significantly when the PbTe well width decreases. Assuming a lattice thermal conductivity of the structure equal to that of bulk PbTe, the enhancement of ZT was entirely explained by the increase in the two-dimensional electronic density of states (42). A reduction in the thermal conductivity for heat flow parallel to the layers in the MQW structure as observed in GaAs–AlAs superlattices would lead to a further increase in the ZT values in the IV–VI MQW structures.

SUMMARY

The special structural, electronic, and optical properties of the IV–VI semiconductors as compared to other semiconductor
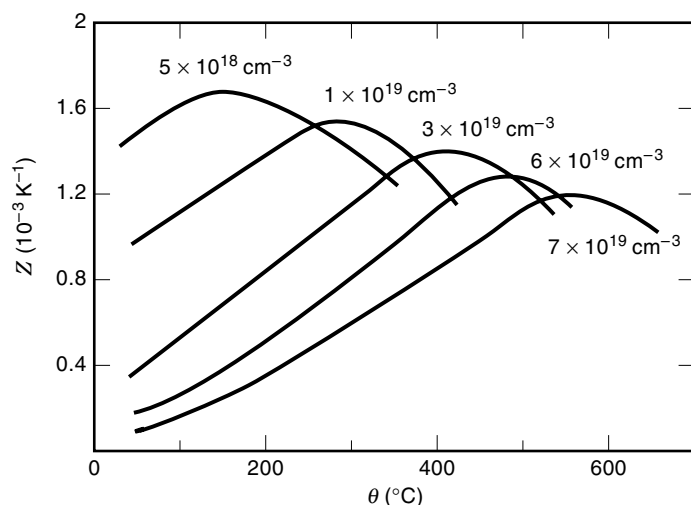
Figure 14. Thermoelectric figure of merit Z versus temperature for n-type PbTe with various doping concentrations.

materials are a consequence of the ten valence electrons per atomic pair instead of the eight valence electrons typical for the tetrahedrally bonded group IV, III–V, and II–VI semiconductors. The most important group of IV–VI materials are the so-called lead chalcogenide (lead salt) compounds and their ternary and quaternary alloys, which are used for applications as infrared detectors, mid- and far-infrared laser diodes, and thermoelectric devices. Their electronic band structure, with the narrow direct minimum gap not at the center but at the edges of the Brillouin zone (L points), has great advantages in particular for achieving infrared pn-junction lasing operating at comparatively high temperatures. Furthermore, high-sensitivity infrared detectors, including focal plane array detectors, can be fabricated with comparatively low-cost technologies.

BIBLIOGRAPHY

1. F. Braun, Über die Stromleitung durch Schwefelmetalle, *Ann. Phys. Chem.,* **153**: 556–563, 1874.

2. J. F. Butler et al., PbTe diode lasers, *Appl. Phys. Lett.,* **5**: 75–77, 1964.

3. H. Preier, Physics and applications of IV–VI compound semiconductor lasers, *Semicond. Sci. Technol.,* **5**: S12–S20, 1990.

4. G. Mahan and O. J. Sofo, The best thermoelectric, *Proc. Natl. Acad. Sci. U.S.A.,* **93**: 7436, 1996; G. Mahan, B. Sales, and J. Shrap, Thermoelectric materials: New approaches to an old problem, *Phys. Today,* March 1997, p. 42.

5. H. Kawamura, Phase transitions in IV–VI compounds, in W. Zawadski (ed.), *Narrow Gap Semiconductors: Physics and Applications,* Berlin: Springer-Verlag, 1980, pp. 470–494.

6. G. Lucrovsky, R. M. Martin, and E. Burstein, Structure, bonding and lattice dynamical properties of the IV–VI compounds, in S. Rabii (ed.), *Physics of IV–VI Compounds and Alloys,* New York: Gordon and Breach, 1974, pp. 93–102.

7. Y. I. Ravich, B. A. Efimova, and I. A. Smirnov, *Semiconducting Lead Chalcogenides,* New York: Plenum, 1970.

8. R. Dalven, Electronic Structure of PbS, PbSe, and PbTe, in F. Seitz, D. Thurnbull, and H. Ehrenreich (eds.), *Solid State Physics,* Vol. 28, New York: Academic, 1973, p. 179.

9. G. Nimtz, IV–VI compounds, in K. Hellwege and O. Madelung, Landolt-Börnstein (eds.), *Numerical Data and Functional Relationships in Science and Technology,* Landolt-Börnstein New Series, Group III, Vol. 17, Part F, Berlin: Springer-Verlag, 1993, pp. 152–180.

10. F. J. Schmitte, IV–VI compounds, in K. Hellwege and O. Madelung, Landolt-Börnstein (eds.), *Numerical Data and Functional Relationships in Science and Technology,* Landolt-Börnstein New Series, Group III, Vol. 17, Part F, Berlin: Springer-Verlag, 1993, pp. 146–152.

11. D. L. Partin and J. Heremans, Growth of narrow bandgap semiconductors, in T. S. Moss and S. Mahajan (eds.), *Handbook on Semiconductors,* Vol. 3A, Amsterdam: North-Holland, 1994, p. 369.

12. B. Schlicht, IV–VI compounds: Solid solutions, in K. Hellwege and O. Madelung (eds.), *Numerical Data and Functional Relationships in Science and Technology,* Landolt-Börnstein New Series, Group III, Vol. 17, Part F, Berlin: Springer-Verlag, 1993, pp. 181–190.

13. W. Jantsch, Dielectric properties and soft modes in semiconducting (PbSnGe)Te, *Springer Tracts Mod. Phys.,* **99**: 1–50, 1983.

14. E. M. Logothetis and H. Holloway, Native defect equilibria and carrier mobilities in lead chalcogenides, in S. Rabii (ed.), *Physics of IV–VI Compounds and Alloys,* New York: Gordon and Breach, 1974, pp. 153–165.

15. G. Bauer and H. Krenn, Lead Selenide, Lead telluride, in E. D. Palik (ed.), *Handbook of Optical Constants,* New York: Academic, 1985, pp. 517–523, 535–546.

16. J. N. Zemel, J. D. Jensen, and R. B. Schoolar, Electrical and optical properties of epitaxia films of PbS, PbSe, PbTE and SnTe, *Phys. Rev.,* **140**: A330, 1965.

17. S. Yuan et al., Electronic and optical properties of PbTe/Pb$_{1-x}$Eu$_x$Te multiple-quantum well structures, *Phys. Rev. B,* **49**: 5476, 1994.

18. T. C. Harman, Control of imperfections in crystals of Pb$_{1-x}$Sn$_x$Te, Pb$_{1-x}$Sn$_y$Se, PbS$_{1-x}$Se, in S. Rabii (ed.), *Physics of IV–VI Compounds and Alloys,* New York: Gordon and Breach, 1974, pp. 141–152.

19. H. Heinrich, Defects in IV–VI compounds, in W. Zawadski (ed.), *Narrow Gap Semiconductors: Physics and Applications,* Berlin: Springer-Verlag, 1980, p. 407.

20. A. J. Strauss, Effect of Pb- and Te-saturation on carrier concentrations in impurity-doped PbTe, *J. Electron. Mat.,* **2**: 553, 1973.

21. J. Baars, Non-tetrahedrally bonded semiconductors, IV–VI compounds, in K. Hellwege and O. Madelung (eds.), *Numerical Data and Functional Relationships in Science and Technology,* New Series, Group III, Vol. 17, Part F, Berlin: Springer-Verlag, 1993.

22. I. Melngailis and T. C. Harman, Single crystal lead-tin chalcogenides, in R. Willardson and A. C. Beer (eds.), *Semiconductors and Semimetals,* New York: Academic Press, 1979, p. 111.

23. H. Preier, Recent advances in lead-chalcogenide diode lasers, *Appl. Phys.,* **20**: 189–206, 1979.

24. A. Lopez-Otero, Hot wall epitaxy, *Thin Solid Films,* **49**: 3, 1978.

25. H. Holloway, Thin film IV–VI semiconductor photodiodes, in G. Hass and M. F. Francombe (eds.), *Physics of Thin Films,* Vol. 11, New York: Academic Press, 1980, pp. 105–203.

26. G. Springholz, Z. Shi, and H. Zogg, Molecular beam epitaxy of IV–VI semiconductors, in M. Santos (ed.), *Heteroepitaxial Thin Film Systems,* Singapore: World Scientific, 1998.

27. D. Partin, Lead salt quantum effect structures, *IEEE J. Quantum Electron.,* **24**: 1716–1726, 1988.

28. G. Bauer et al., IV–VI quantum wells for infrared lasers, *J. Nonlinear Opt. Phys. Mater.,* **4**: 283–312, 1995.

29. A. Katzir et al., Tuneable lead salt lasers, in P. K. Cheo (ed.), *Handbook of Solid State Lasers,* New York: Marcel Dekker, 1989, p. 228.

30. H. Holloway and G. Jesion, Lead strontium sulfide and lead calcium sulfide, two new alloy semiconductors, *Phys. Rev. B,* **26**: 5617, 1982.

31. Z. Shi et al., Midinfrared lead salt multi-quantum well diode lasers with 282 K operation, *Appl. Phys. Lett.,* **66**: 2537–2539, 1995.

32. G. Bauer and W. Jantsch, PbTe-doping superlattices—physics and applications, in *Quantum Well and Superlattice Physics II, Proc.* SPIE, **943**: 1988, pp.107–113.

33. Litton Electron Devices, Tempe, AZ 85281.

34. A. M. Andrews et al., Backside-illuminated $Pb_{1-x}Sn_xTe$ heterojunction-photodiode, *Appl. Phys. Lett.,* **26–28**: 438, 1975.

35. D. K. Hohnke et al., Thin film (Pb,Sn)Se photodiodes for 8–12 μm operation, *Appl. Phys. Lett.,* **29–31**: 98, 1976.

36. H. Zogg et al., Photovoltaic IV–VI on Si infrared sensor arrays for thermal imaging, *Opt. Eng.,* **34**: 1946, 1995.

37. M. Tacke, New developments and applications of tunable IR lead salt lasers, *Infrared Phys. Technol.,* **36**: 447–463, 1995.

38. Z. Feit et al., Low threshold PbEuTe/PbTe separate confinement buried heterostructure diode lasers, *Appl. Phys. Lett.,* **68**: 738–740, 1996.

39. G. Scarmarcio et al., High power infrared ($\lambda \sim 8$ μm) superlattice lasers, *Science,* **276**: 773–776, 1997, and references cited therein.

40. H. K. Choi et al., 175K continuous wave operation of InAsSb/InAlAsSb quantum well diode lasers emitting at 3.5 μm, *Appl. Phys. Lett.,* **68**: 2936–2938, 1996.

41. G. Chin et al., Stabilizing lead-salt diode lasers: Understanding and controlling chaotic frequency emission, *Science,* **274**: 1498–1501, 1996.

42. L. D. Hicks et al., Experimental study of the effect of quantum-well structures on the thermoelectric figure of merit, *Phys. Rev. B* **53**: R10493, 1996.

GUNTHER SPRINGHOLZ
GÜNTHER BAUER
Johannes Kepler Universität Linz

SEMICONDUCTORS AND HETEROSTRUCTURES.

SEMICONDUCTORS, MAGNETIC. See MAGNETIC

SEMICONDUCTORS, ORGANIC. See ORGANIC SEMI-

SEMICONDUCTORS, III–VI. See III–VI SEMICON-

SEMICONDUCTOR SWITCHES. See PHOTOCONDUCT-